Cement and Concrete Composites 143 (2023) 105265

Contents lists available at ScienceDirect

Cement and Concrete Composites

journal homepage: www.elsevier.com/locate/cemconcomp

Understanding the thermal behavior of geopolymeric composites designed by packing model

Y. Luo [a], C.H. Koh [a], S.H. Li [b], H.J.H. Brouwers [a], Qingliang Yu [a,b,*]

[a] *Department of the Built Environment, Eindhoven University of Technology, P.O. Box 513, 5600MB, Eindhoven, the Netherlands*
[b] *School of Civil Engineering, Wuhan University, 430072, Wuhan, PR China*

ARTICLE INFO

Keywords:
Geopolymer composite
Lightweight
Packing
Thermal behavior
High temperature

ABSTRACT

The interaction between geopolymer binder and aggregates has a significant impact on thermal performance, which however still lacks sufficient understanding. In this study, a novel approach for designing high temperature resistant geopolymer composites is introduced. The microstructural-thermophysical properties and heat transfer pattern of the developed geopolymer composites are investigated and further linked to the progressive evolution up to 800 °C. Results reveal that the optimized packing contributes to a significantly high porosity from 48.6% to 52.8% and large moisture permeability in lightweight aggregate incorporated geopolymer (LWAG). A much lower thermal conductivity but comparable mechanical strength is achieved in LWAG as compared to sand aggregate incorporated geopolymer (SAG). At elevated temperatures, sand incorporation results in a fast heat transfer, and lightweight aggregates lead to a large temperature gradient within geopolymer composites. Compared to SAG, LWAGs show a lessened microstructural degradation with noticeable strength gain at 800 °C. Increasing the distribution modulus from 0.2 to 0.3 eases the thermal deterioration thanks to the decreased temperature gain rate and thermal diffusivity, resulting in low thermal shrinkage and high residual strength.

1. Introduction

Geopolymer has emerged as an environmentally sustainable binder material in the last few years, which is recognized as a promising alternative to ordinary Portland cement (OPC), especially for applications requiring thermal stability [1,2]. Generally, geopolymer is mainly derived from pozzolanic or aluminosilicate sources, which involve in the alkali activation or acidic activation process [2–5]. Among these, the common geopolymer is produced by alkaline activating Class F fly ash (FA), resulting in a three-dimensional aluminosilicate structure. It enables a superior level of mechanical property and structural integrity after exposure to high temperatures, as compared to OPC concrete [6,7]. Since the excellent thermal behavior of geopolymer binders has been extensively verified, there is a growing research interest in designing high temperature resistant geopolymeric composites for large-scale applications.

Zhang et al. [8] and Ali Bagheri et al. [9] compared geopolymer and OPC-based mortar/concrete with sand aggregates, and reduced thermal degradation of compressive strength is observed in geopolymer composites due to the superior thermal stability of geopolymeric gel. Çelikten et al. [10] studied the microstructural properties of geopolymer mortar exposed to high temperatures and found that the interfacial transition zone between the geopolymeric binder and sand is weakened with temperature increase. Kong et al. [11,12] and Rickard et al. [13] investigated geopolymer composites with sand, basalt, slag, and lightweight aggregates (LWA), and concluded that the thermal expansion incompatibility between binder and aggregates plays crucial roles in structural and strength deterioration of geopolymer composites at elevated temperatures. According to previous works, the interaction between geopolymer binder and aggregates plays an important role in determining the thermal performance of geopolymer composites. The incorporation of aggregates with different characteristics, such as inert property, density, and particle size, varies the pore structure as well as the total porosity of composites. Besides, it not only alters the thermophysical properties such as thermal conductivity and thermal diffusivity but also affects the thermal stress and bonding mechanism within geopolymer composites on exposure to elevated temperatures [14–16]. Ultimately, it both influences and potentially complicates the thermal behavior of the resultant geopolymer composites. However, limited attention has been devoted to exploring the correlation between geopolymeric binder-aggregate interaction and initial properties, including microstructure and thermophysical characteristics. Consequently, the

---

* Corresponding author. Department of the Built Environment, Eindhoven University of Technology, P.O. Box 513, 5600MB, Eindhoven, the Netherlands.
E-mail address: q.yu@bwk.tue.nl (Q. Yu).

https://doi.org/10.1016/j.cemconcomp.2023.105265
Received 16 May 2023; Received in revised form 15 August 2023; Accepted 20 August 2023

subsequent impact of these factors on the thermal behavior of geopolymer composites remains unexplored.

On the other hand, it is widely accepted that the durability of cementitious composites is strongly linked to the packing of granular ingredients. Brouwers and Radix [17] first applied a modified Andreasen and Andersen (A&A) particle packing model to design concrete mixture ingredients, including powders, fine aggregate, and coarse aggregate. The rheology and mechanical properties of the concrete mixture were optimized by achieving a high packing density and homogeneity. Based on that, self-compacting concrete (SCC) [17,18], ultra-high-performance concrete (UHPC) [19,20], earth-moist concrete [21,22], and ultra-lightweight concrete (ULWC) [23–25] were developed. Nevertheless, limited attention has been given to applying the packing model to design composites for thermal application. Yu et al. [26] applied the modified A&A model to optimize the packing of LWA in gypsum-based composite and obtained a good balance between thermal conductivity and mechanical properties. Superior thermal stability was testified as compared to traditional gypsum board. It refers that the packing of ingredients alters the thermophysical properties and further influences the thermal behavior of the resultant composites. In particular, when applying LWA with high inert porosity, the modified A&A model can be used to design the porosity and pore size distribution of the component, hence tailoring the thermophysical properties. It is possible that, by optimizing the particle packing of geopolymer based composite, better thermal performance can be achieved. However, in the realm of designing geopolymer-based materials for thermal applications, existing studies have predominantly focused on raw materials, alkali activators, and the selection of fibers or aggregates. To the best knowledge of the authors, no studies have been reported concerning the role of aggregate packing in determining the thermal performance of geopolymers.

In light of the above research gaps, a packing theory is introduced to develop geopolymer composites with normal quartz sand and LWA. The effect of geopolymeric binder-aggregate interaction on the initial properties, such as microstructural formation, thermophysical properties, and mechanical strength, are systematically characterized. Based on the acquired properties, a simulation is carried out to numerically explore the heat transfer pattern within geopolymer composites. Ultimately, the initial properties and heat transfer patterns of geopolymer composites are further linked to the high temperature behavior, including post-heating thermal conductivity, microstructure/volumetric stability, and residual strength. The novelty of this work lies in clarifying the interrelationships among microstructural-thermophysical properties, heat transfer patterns, and the high temperature behavior of geopolymer composites. Additionally, it provides a comprehensive understanding of the progressive evolution of geopolymer composites under high temperatures, which is essential for revealing the thermal degradation mechanism of geopolymer-based mortar and concrete.

2. Experimental program

2.1. Materials

In this study, low calcium (class F) fly ash (FA) and ladle slag (LS) were applied as binder materials. Class F FA was purchased from Vliegasunie, The Netherlands. LS was directly collected from stockpiles of Tata Steel, The Netherlands. Before application, LS was ground using a disk mill to obtain a suitable particle size distribution. The average particle size (d50) of FA and LS are around 16.00 μm and 13.99 μm respectively as determined by a laser particle size analyzer (Mastersizer 2000, Malvern Instruments, UK). The detailed particle size distributions (PSD) of all applied solid materials are shown in Fig. 1. The chemical composition of FA and LS are given in Table 1, as determined by X-ray fluorescence spectrometry (XRF) (PANalytical Epsilon 3). The loss on ignition has been measured from 105 °C to 1000 °C. Commercially available sodium hydroxide (NaOH) pellets (analytical level) and sodium silicate (Na_2SiO_3) solution (27.69 wt% SiO_2, 8.39 wt% Na_2O, and 63.9 wt% H_2O) were used.

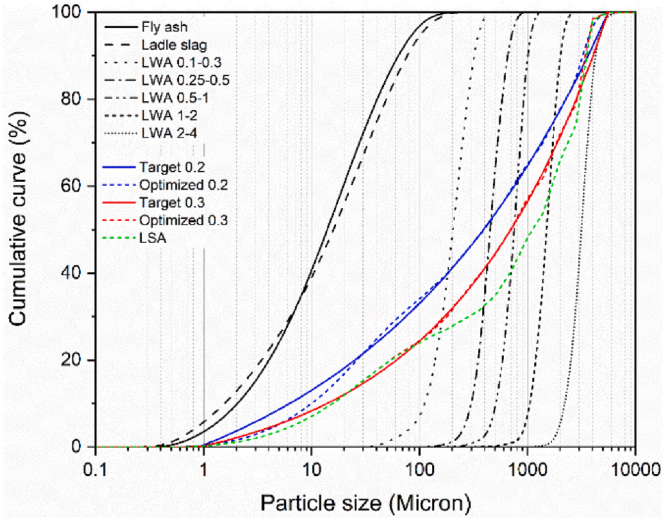

Fig. 1. PSDs of the solid materials, the target lines, and the resulting integral grading lines of mixtures with different distribution modulus.

Commercially available mineral granulates, ROTOCELL PLUS® is applied in this work as lightweight aggregate (LWA) with five different size fractions of 0.1–0.3 mm, 0.25–0.5 mm, 0.5–1 mm, 1–2 mm, and 2–4 mm. The PSDs of LWA in different size fractions are presented in Fig. 1. The physical and chemical properties given by the producer are listed in Table 2. The applied LWA is produced from highly porous expanded silicate as shown in Fig. 2, exhibiting ultra-low bulk density and good thermal stability up to 1000 °C. In addition, normal sand with different size fractions of 0.1–0.3 mm, 0.3–0.5 mm, 0.5–1 mm, 1–2 mm, and 2–4 mm was used as normal weight aggregate compared to LWA. The specific density of normal sand is around 2575 kg/m^3 (see Fig. 3).

2.2. Mix design methodology

For room temperature applications, for instance, a high mechanical strength matrix always requires a dense structure with low porosity. Nevertheless, under high temperatures, the dense structure with low permeability impedes thermally induced water evaporation, resulting in high thermal stress and severe structural deterioration [27]. Herein, the design target is to develop a geopolymer composite with a good balance between room temperature properties and elevated temperature performance. A packing design is proposed to optimize the accumulation of solid particles including solid precursors and aggregates, and hence obtain a dense matrix with good packing of particles. By applying a highly porous LWA into the packing model, a porous matrix with high permeability but less flaw or closed pores can be designed.

In the present study, the target integral grading curve was determined following the modified Andreasen and Andersen (A&A) model [28], reading:

$$P(D) = \frac{D^q - D^q_{min}}{D^q_{max} - D^q_{min}} \tag{1}$$

Where $P(D)$ is referred to the cumulative fraction of total particles being smaller than size D, D is the particle size (μm), D_{min} and D_{max} are the minimum and maximum particle size (μm) respectively, and q represents the distribution modulus. Based on that, the mix proportion was calculated following:

$$RSS = \sum_{i=1}^{n} \left[P_{mix}\left(D_i^{i+1}\right) - P_{tar}\left(D_i^{i+1}\right) \right]^2 \rightarrow min \tag{2}$$

The RSS represents the sum of the squares of the residuals P_{mix} is the composed mix, P_{tar} is the target grading curve obtained from Eq. (1). To

Table 1
Chemical composition and loss on ignition.

Oxide (wt.%)	SiO_2	Al_2O_3	CaO	Fe_2O_3	MgO	SO_3	K_2O	Others	LOI (1000°)
Fly ash	54.57	21.60	6.12	9.04	1.17	0.41	2.85	2.13	2.11
Ladle slag	2.1	24.6	56.75	3.12	2.24	0.61	–	1.16	9.42

Table 2
The physical-chemical properties of applied lightweight aggregates.

Type	0.1–0.3 mm	0.25–0.5 mm	0.5–1 mm	1–2 mm	2–4 mm
Physical properties					
Bulk density (kg/ m^3)	400 ± 15%	365 ± 15%	330 ± 15%	310 ± 15%	300 ± 15%
Particle density (kg/m^3)	700	700	600	550	500
Average grain strength (N/mm^2)	22	18	18	18	12
Melting point in °C	1000				
Chemical composition					
SiO_2	55.0%				
Al_2O_3	22.0%				
$K_2O + Na_2O$	12.0%				
Fe_2O_3	3.0%				
CaO	2.0%				
MgO	1.0%				
TiO_2	0.5%				
LOI (1000 °C)	4.0%				

optimally approach the target particle grading curve, an optimization algorithm namely, the Least Squares Method (LSM) was applied to adjust the proportion of each solid material until the RSS is minimal. The optimization algorithm was fulfilled by applying the solver tool in Microsoft Excel@. In the applied packing model, the distribution modulus determines the relative proportion of fine particles and coarse particles. According to Hüsken and Brouwers [21], a coarser mixture can be obtained with a higher distribution modulus and vice versa. For the geopolymeric system, Borges et al. [29] and Gao et al. [30] proposed an optimum q value of around 0.23, accounting for factors such as packing density and mechanical strength. In the present study, to investigate the effect of packing patterns on the high temperature behavior of geopolymer based concrete, two distribution moduli (0.2 and 0.3) were adopted. The target particle grading curve and optimized grading curve with two distribution moduli were calculated respectively as depicted in Fig. 1, and the accordant solid materials proportion of the mixtures (named L-2 and L-3) is shown in Table 3. Moreover, to study the effect of the packing principle as well as aggregate size distribution, a mixture with un-optimized packing (denoted as L-L) was designed based on Mix 2 by manually adjusting the aggregate size distribution towards a higher fraction of big aggregates while keeping aggregate vol% as constant, as also presented in Fig. 1. An optimized mixture (denoted as S-3) with normal sand as aggregate was prepared to compare with L-3.

In terms of the geopolymeric binder design, a by-product of steel manufacturing, ladle slag (LS), is incorporated to regulate the workability in avoiding the sedimentation/floatation of aggregates. Besides, the incorporation of LS is clarified to promote the thermal performance of geopolymer binders according to our previous study [31]. In all mixtures, the binder was blended by FA and LS at a mass ratio of 85 to 15, and the silicate modulus (SiO_2/Na_2O mol. ratio), as well as equivalent Na_2O wt.%, were set as 1.5 and 6 wt% respectively according to Ref. [31]. To ensure acceptable workability without the addition of superplasticizer, a fixed w/c ratio of 0.4 was adopted. The water content included the water in sodium silicate solution and extra distilled water.

2.3. Sample preparation

The activator was prepared by mixing sodium hydroxide pellets, sodium silicate solution, and distilled water. The mass ratio of 0.14 between NaOH pellets and sodium silicate solution was used to achieve the desired silicate modulus, equivalent Na_2O wt.%. Distilled water was applied to tailor the water/binder ratio. The activator was cooled at ambient temperature for 24 h before use.

Table 3
The proportion of mix designed applying the packing model (per m^3).

Material		L-2	L-3	L-L	S-3
Binder	Total	605.3	462.5	462.7	462.5
	FA (85 wt%)	514.5	393.1	393.3	393.1
	LS (15 wt%)	90.8	69.4	69.4	69.4
Aggregate	0.1-0.3	28.4	36.6	13.0	244.3
	0.25-0.5	22.8	22.9	16.9	166.6
	0.5–1	22.1	27.1	29.9	211.4
	1–2	28.8	35.7	43.0	298.6
	2–4	46.7	64.6	81.3	569.9
Activator		337.2	257.6	257.7	257.6
Si modulus*		1.5	1.5	1.5	1.5
Na_2O%**		6.0	6.0	6.0	6.0
w/c		0.4	0.4	0.4	0.4
Distribution modulus		0.2	0.3	–	0.3
Aggregate vol%		45.9	57.9	57.9	57.9

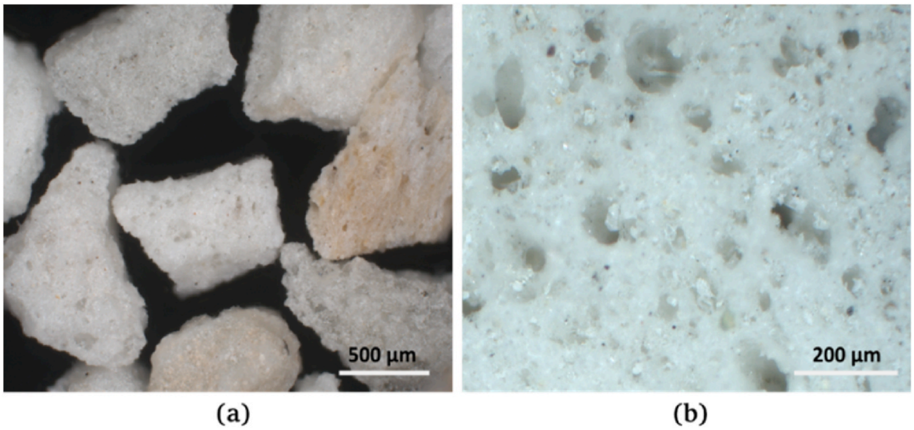

Fig. 2. Structure of LWA: (a) surface and (b) pore structure.

A 5L Hobart mixer was applied to prepare geopolymer composites. Firstly, the solid precursors and aggregates smaller than 2 mm were added in a mixer and mixed for 1 min until a homogeneous state has been reached. Then, the activator was slowly added while stirring at a low speed for 30 s. Afterward, the aggregate fraction between 2 and 4 mm was added slowly, following another 60 s at a high-speed stirring. After mixing, the fresh mixtures were immediately poured into 40 × 40 × 160 mm^3 molds and slightly vibrated for 30 s. The samples were sealed with plastic foil and stored at room temperature (20 ± 2 °C) for 24 h before another 24 h of 60 °C curing. Subsequently, the samples were demoulded and cured at room temperature under sealed conditions for 26 days until characterization.

2.4. Testing methods

2.4.1. Basic properties

For the measurement of density, porosity, Micro-computed tomography (Micro-CT), scanning electron microscopy (SEM), thermal transport properties, and water vapor properties, the tested samples were cut from the core part of specimens at 28 days of curing and immersed in isopropanol for 72 h to cease the hydration, following a 24 h 40 °C drying.

- Scanning electron microscopy (SEM)

The microstructure was observed by applying Phenom Pro (The Netherlands). The tested samples were cut from the center of prisms and impregnated with epoxy resin. Subsequently, the samples were polished and coated with Au by using a Quorum 150 TS plus sputter coater. The observation was performed in a Backscattered electron (BSE) mode with an accelerating voltage of 15 kV.

- Density and porosity

The porosity, φ of the obtained samples was calculated following

$$\varphi = \left(1 - \frac{\rho_b}{\rho_s}\right) \tag{3}$$

here ρ_s represents the skeleton density, and ρ_b refers to the bulk density. Among these, the skeleton density was determined using a Micromeritics AccuPyc II 1340 Pycnometer, and the bulk density was calculated from the mass and volume of cubic samples.

- Micro-computed tomography (Micro-CT)

Micro-CT was performed on cubic samples (10 × 10 × 40 mm^3) to characterize the pore size distribution. During the measurement, a voltage of 70 Kv with a current of 200 mA was applied to achieve a pixel resolution of 6.6 μm. To obtain a representative result, 634 images from a 4.18 mm thickness of section were obtained, and three different sections for each sample were analyzed. The data were combined and visualized as shown in Fig. 1, and then the pores were extracted to calculate the pore size distribution. The volume of 140 mm^3 was tested for different samples, and the pore size between 6.6 and 660 μm was detected.

- Thermal transport properties

The thermal transport parameters including thermal conductivity λ, thermal diffusion α, and volumetric heat capacity $C_{p,v}$ were measured by a Hot Disk thermal constants analyzer (TPS 2500 S, Sweden) at room temperature (20 ± 2 °C), following ISO 22007-2 [32]. Before measurement, the samples (40 × 40 × 20 mm^3) are dried at 40 °C until a constant weight is reached. A transiently heated plane sensor (Hot Disk 8563 F2 Kapton sensor, capable of operating up to 300 °C) was placed in between two slices of the identical sample with a smooth surface or directly inserted into aggregates, acting as the heat source and dynamic temperature sensor. The measurement time was set as 80 s and the heating power was 70 mW. Three measurements were carried out on each sample and the average data was recorded. The apparatus accuracy is ±2% for thermal conductivity measurement and ±7% for specific heat measurement.

- Water vapor transmission

To determine the water vapor transmission within specimens, the dry cup method was performed according to standard ASTM E96 [33]. The specimens in size of 40 × 40 × 40 mm^3 were applied. Before the measurement, the edges of specimens were thoroughly sealed with plastic film and wax to prevent vapor through the edges. The sealed samples were attached to the cups filled with anhydrous calcium chloride and then placed in a humidity chamber at 20 °C, 50% RH. The change of weight (Δm) at a successive time (Δt) is collected by weighing the cups over a specific period. Six consecutive weighings were recorded when the weight change rate of specimens reached a steady state. The water vapor transmission rate (WVTR) was calculated according to:

$$WVTR = \frac{\Delta m}{A \bullet \Delta t} \tag{4}$$

where A is the test area, used as 0.0016 m^2. The permeability, δ was calculated following:

$$\delta = \frac{WVTR}{\Delta p} \bullet thickness \tag{5}$$

where Δp represents the vapor pressure difference, used as 8.77 mm Hg at 20 °C, 50% RH, and thickness is 0.04 m.

- Compressive strength

The compressive strength test was conducted following EN 196-1 [34]. 3 parallel prismatic samples (40 × 40 × 160 mm^3) were tested at 28 days of curing for compressive strength. The prisms were halved by applying the three-point loading method. Afterward, 6 fractured parts were tested under a loading rate of 2400 N/s. The recorded strength was obtained by the average value.

2.4.2. Heat transfer study

Two modeling setups are incorporated in the heat transfer study, refer to Fig. 4a. The aggregates and binder are modeled separately in the component's setup (denoted as 'CS') model; the properties of the aggregates (denoted as 'agg') are measured, while the properties of the geopolymer binder (denoted as 'bind') are calculated. The 'bulk setup (denoted as 'BS') model depicts the composite as a single bulk body, where its material properties are measured directly from the overall composite (denoted as 'comp'). The CS model is used to study the influence of aggregates in the composite, while the BS model is used to validate the CS model. The comparison of modeling output between 'CS' model and 'BS' model is given in Appendix Fig. A1.

2.4.2.1. Set up of geometry. To set up the composite geometry for CS study, models are represented two-dimensionally. The aggregate is portrayed as a sphere with a diameter d_{agg} after averaging out their irregular shapes and represented as a circle in two dimensions, refer to Fig. 4b. In addition, the volume fraction of aggregates in the composite $\%V_{agg}$ is converted into area fraction $\%A_{agg}$ in two-dimension. The aggregates are represented by their mean diameter d_{agg}, with five different categories of aggregate size included in the model. The overall geometry setup is presented in Fig. 5, it should be noted that identical geometry is applied for L-3 and S-3 due to their same packing design. The geometries are generated with MATLAB codes and imported into Comsol

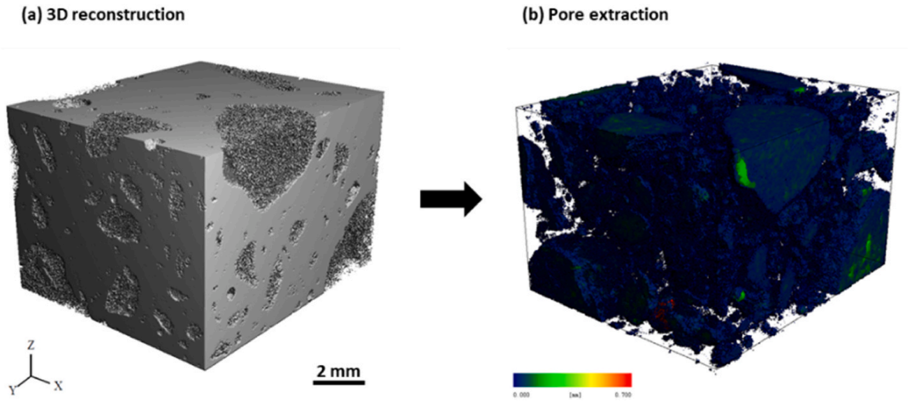

Fig. 3. The reconstruction and visualization of the 3D structure by Micro-CT.

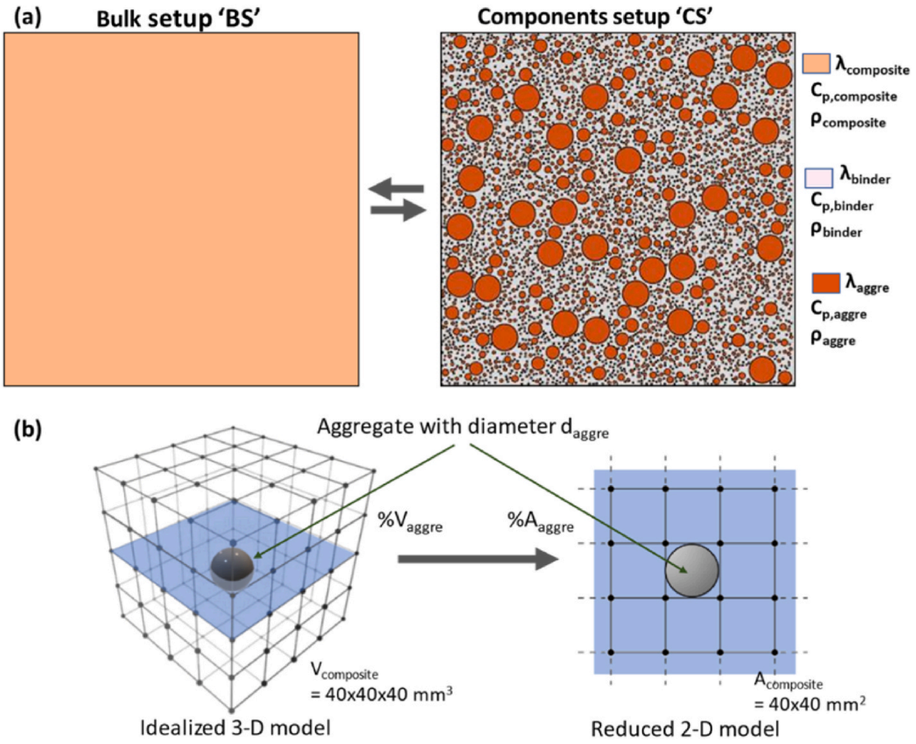

Fig. 4. (a) Model setups and (b) aggregate modeling in the 'CS' model.

Multiphysics for further simulation.

2.4.2.2. Heat transfer modeling. The influence of different packing models on the heat transfer process within the composites is studied using the Comsol Multiphysics 5.6 software. The model is solved using the following heat transport equation [35]:

$$\frac{C_{p,v}}{\rho}\frac{\partial T}{\partial t} - \lambda\left(\frac{\partial^2 T}{\partial^2 x} + \frac{\partial^2 T}{\partial^2 y}\right) = Q \tag{9}$$

where λ is the effective bulk thermal conductivity, $C_{p,v}$ is the measured volumetric heat capacity under constant pressure, ρ is the bulk density, Q is the heat source, and T is the temperature profile to be solved. For practical reasons, λ is assumed to remain constant at the average value. The main input parameters, namely bulk density, thermal conductivity, and volumetric heat capacity for the modeling are determined as follows:

The bulk density of the standalone binder ρ_{bind} is calculated according to:

$$\rho_{bind} = \frac{m_{comp} - m_{agg}}{(1 - \%V_{agg})} \tag{10}$$

where m_{comp} and m_{agg} are the mass of the composite and aggregate respectively, and $\%V_{\text{agg}}$ is the volume fraction of aggregates in the composite.

The thermal conductivity λ_{bind} is obtained by treating the solid and pores in the binder as thermal resistors in parallel [36] with the following equation

$$\lambda_{bind} = (1 - \varphi)\lambda_{solid} + \varphi\lambda_{air} \tag{11}$$

in which, φ is the volume fraction of the air pores (porosity) in the binder, λ_{solid} is calculated from the approximate thermal conductivity of the solid skeleton of a plain FA/LS geopolymer as 0.5480 W/mK, and λ_{air} is the thermal conductivity of air at 0.026 W/mK.

The volumetric heat capacity of binder $C_{p,v,bind}$ is obtained by using a weighted average equation [37]:

Range (mm)	d_{agg} (mm)	L-2				L-3 and S-3				L-L			
		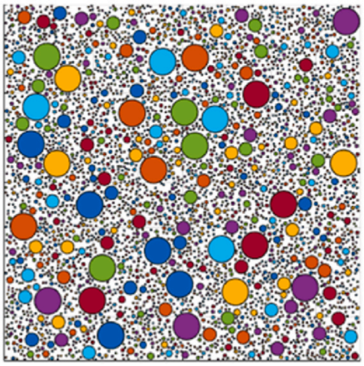				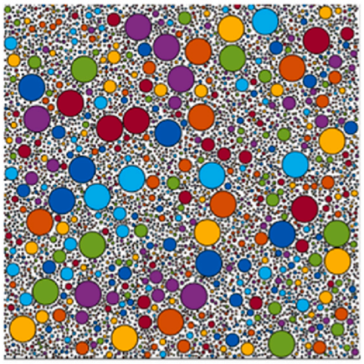				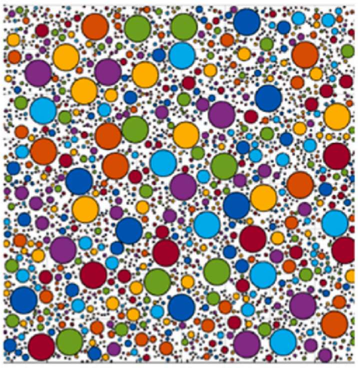			
		$\%V_{agg}$	$n_{V,agg}$	$n_{A,agg}$	$\%A_{agg}$	$\%V_{agg}$	$n_{V,agg}$	$n_{A,agg}$	$\%A_{agg}$	$\%V_{agg}$	$n_{V,agg}$	$n_{A,agg}$	$\%A_{agg}$
2 – 4	3.000	16.1	730	29	12.7	22.2	1007	40	17.5	27.1	1227	48	21.3
1 – 2	1.500	9.3	3363	66	7.3	11.5	4173	82	9.0	13.8	5015	98	10.9
0.5 – 1	0.750	6.7	19422	191	5.3	8.2	23813	234	6.5	9.1	26268	258	7.1
0.25 – 0.5	0.375	6.5	150726	740	5.1	6.5	151318	743	5.1	4.6	107389	527	3.6
0.1 – 0.3	0.200	7.3	1113893	2916	5.7	9.4	1434229	3755	7.4	3.3	496883	1301	2.6
	Total	**45.9**			**36.0**	**57.9**			**45.5**	**57.9**			**45.5**
Mesh elements		993679 (triangles)				1042778 (triangles)				640919 (triangles)			

Fig. 5. Two dimensions geometry setup.

$$\frac{C_{p,v,comp}}{\rho_{comp}} = \%wt._{agg}\frac{C_{p,v,agg}}{\rho_{agg}} + \%wt._{bind}\frac{C_{p,v,bind}}{\rho_{bind}} \tag{12}$$

where $\%wt._{agg}$ and $\%wt._{bind}$ represent the weight percentage of binder and aggregate respectively.

2.4.2.3. External thermal load and output results. Both models are set up with heat transfer from the heat source through their perimeter into the body. Similar to the laboratory setup, heat is transferred from the heating source in an oven to the body by convection and radiation, which can be described by an equivalent heat transfer coefficient h, and the heat source Q_{in} can be described using the following equation:

$$Q_{in} = h(T_{ext} - T) \tag{13}$$

where T_{ext} is the temperature in the oven, and h is set at 10. The heating temperature T_{ext} profile is set as the boundary conditions:

$$\begin{matrix} T_{ext}(x = 0, 0 \le y \le L, t) \\ T_{ext}(x = L, 0 \le y \le L, t) \\ T_{ext}(0 \le x \le L, y = 0, t) \\ T_{ext}(0 \le x \le L, y = L, t) \end{matrix} = \begin{cases} 20 & t = 0 \\ 20 + 10t & 0 < t \le 78\ min \\ 800 & 78 < t \le 138\ min \end{cases} \tag{14}$$

Namely, the sample is heated at a rate of 10 °C/min from 20 °C to 800 °C, and subsequently held at 800 °C for another 60 min to reach the thermal equilibrium. The initial condition of the body is set at 20 °C. A time-dependent solver is used, with a total simulation time of 138 min with a 1-min time-step. The T profiles from six data points are extracted for study: 0 (on the surface), 4, 8, 12, 16, and 20 cm (center) from the surface. The temperature graphical profiles at 10 min intervals are exported to supplement the result analysis.

2.4.3. *High temperature behavior*

- High temperature exposure procedure

The high temperature exposure test was performed in an electric muffle furnace. The prismatic samples (40 × 40 × 160 mm^3) at 28 curing days were heated from room temperature to different temperatures of 100, 200, 400, 600, and 800 °C. According to our previous work [31], a heating rate of 10 °C/min was applied until reaching the target temperature and remaining the temperature for another 1h to achieve a uniform temperature distribution. Then the specimens were naturally cooled down to ambient temperature (20 ± 2 °C) in the furnace and sealed with plastic foil until further characterization. For each composite, three samples were tested under the same condition.

- Thermal volume stability and residual compressive strength

The thermally induced linear shrinkage of samples was determined by comparing the length of the longest side of the prismatic samples before and after thermal exposure. For the residual compressive strength, the cooled prismatic samples were halved using the three-point loading method without being subjected to harmful stress. The halves were tested at a loading rate of 2400 N/s according to the same protocol in Section 2.4.1. For each mixture after specific temperature exposure, the average value of six replicates was recorded as residual compressive strength.

3. Results and discussion

3.1. *Basic characteristics*

3.1.1. *Appearance and microstructure observation*

The cross-section of samples with different aggregates and packing models are presented in Fig. 6. The highlighted white particles and crystalline-like particles represent LWA and sand, respectively, and the dark regions around the particles indicate the binder gel and the black regions denote pores and voids. The aggregates distribute homogeneously in all matrices, indicating the proper workability to avoid aggregate segregation. Notably, a wide range of particle sizes can be observed in developed L-2, L-3, and L-L samples. From L-2 to L-3, with an increasing q value, more LWAs are detected. A coarser packing pattern with a larger proportion of big size aggregates but fewer small size aggregates is obtained in unoptimized sample L-L. The S-3 sample with sand aggregates shows a similar packing pattern as L-3 because of the same q value in the mix design. Moreover, pores and voids are formed in all specimens caused by air entrainment during the mixing.

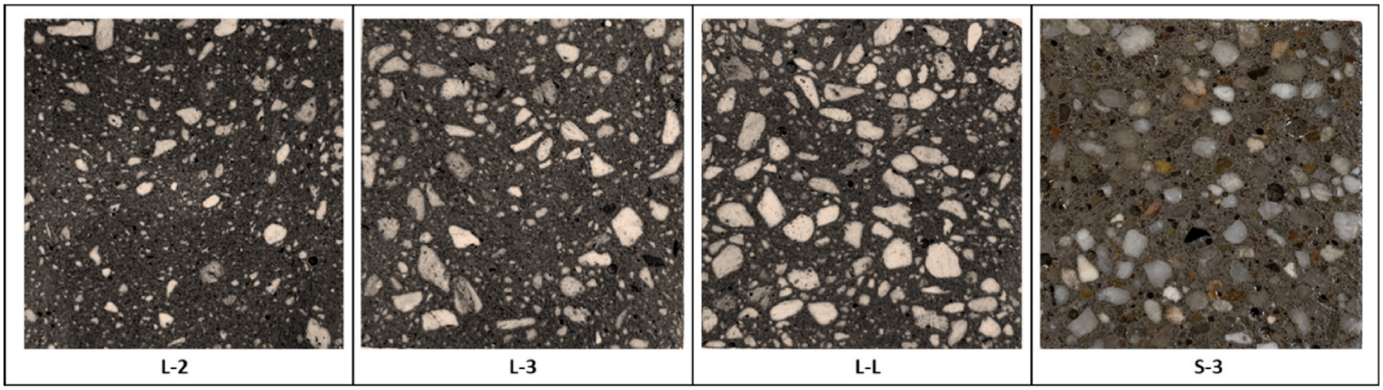

Fig. 6. The cross-section of samples with LWA and sand aggregates.

The interface between binder gel and aggregates is presented in Fig. 7. In Fig. 7a and b, the dense regions with spherical FA particles are identified as geopolymer binder whilst the extremely porous structures are referred to as LWAs. A well-connected interfacial transition zone (ITZ) between paste and LWAs is observed, which should be attributed to the impregnation of binder gel into the porous surface of LWAs that forms an interlocked bonding. While a poorer connection is noticed between binder and sand aggregates in Fig. 7c and d.

3.1.2. *Density and porosity*

Fig. 8 depicts the bulk density and porosity of the geopolymer composites. In general, the SAG sample has a significantly high density of 1.99 g/cm^3 and low porosity of 24.55% as compared to LWAGs. The incorporation of LWA largely decreases the density to 1.21 g/cm^3 and increases the porosity to 48.63% in L-2. In addition, when increasing the q value from 0.2 to 0.3, the density is further decreased with higher porosity. This is because the increased q value leads to a higher LWA amount while a reduction in binder content as can be known from Table 3. Notably, a lower density with higher porosity is obtained in unoptimized sample L-L as compared to L-3, despite the aggregate vol% being kept the same as L-3. This can be attributed to both the poor packing quality in L-L and the higher fraction of big aggregates in L-L as compared to L-3, which potentially introduces more pores. The porosity from the binder and aggregate are further calculated and summarized in Table 4. It is clear that a higher q value leads to a lower binder porosity but a higher aggregate porosity, and the unoptimized L-L samples have higher aggregate porosity. Moreover, it should be noted that the highest binder porosity of 20.44% resulted in S-3. It is ascribed to the poor workability in SAG due to the water absorption from the sand.

The detailed pore structure of geopolymer composite is investigated by microtomography technology (Micro-CT) as presented in Fig. 9. The calculated porosity is 14.0%, 22.4%, 30.1%, and 7.6% for L-2, L-3, L-L, and S-3 respectively. Here, the calculated porosity is lower than the total porosity, resulting from the limited pore size detected range (>6.6 μm) of Micro-CT. In general, the variation trend correlates well with that of total porosity in different composites, and the calculated results can be used as an indicator for understanding the influence of different aggregates and packing designs on pore structure. The PSD in LWAG shows

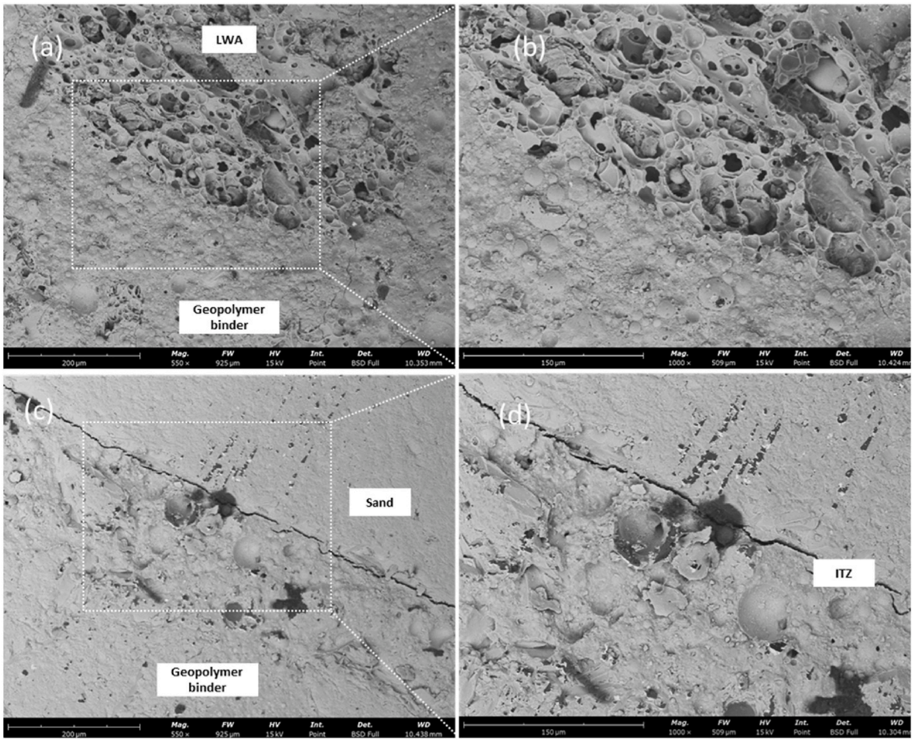

Fig. 7. SEM image of geopolymer binder and aggregate interface.

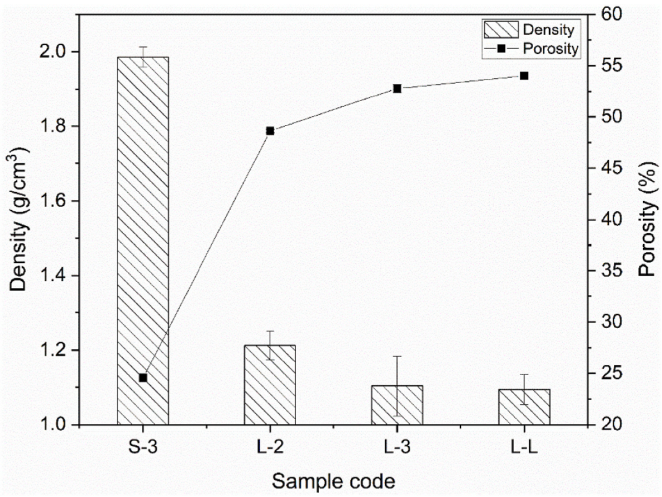

Fig. 8. The density and porosity of the geopolymer composites.

Table 4
Calculated porosity of binder and aggregate in different mixes.

Sample code	φ_{Bind}	φ_{Agg}	φ_{Total}
L-2	8.06	40.57	48.63
L-3	2.49	50.3	52.79
L-L	2.8	51.22	54.02
S-3	20.44	4.11	24.55

a parabolic shape with the main peak, while the SAG has a widely distributed size of pores. The pores detected in S-3 are mainly from the binder, which is related to poor workability. In LWAG, with the q value change from 0.2 to 0.3, the main peak shifts from 34.6 to 40.9 μm with an increased peak intensity and wider pore size range, resulting in a coarser pore structure. As compared to L-3, the L-L sample shows both higher main peak intensity and a higher fraction of big pores/defects (larger than 100 μm), which explains its higher porosity as compared to L-3.

3.1.3. Water vapor properties

Water vapor transport plays an important role in determining the thermal stability of building materials since it represents the ability to transfer water vapor from the body at high temperatures. The water vapor transmission along with time is shown in Fig. 10, and the transport properties are calculated and summarized in Table 5. It can be seen that the introduction of LWAs results in a much higher water vapor transport and permeability than that of SAG owing to the higher porosity and pore openness. However, among LWAGs, it is interesting to notice that the water vapor transport, as well as permeability, are negatively related to the total porosity of the composites. The L-3 and L-L with the highest porosity show the lowest water vapor transmission and permeability. Because water vapor transport is mainly determined by pore connectivity, it is most likely the LWAs are largely composed of closed/isolated pores. Thus, despite the high porosity, the higher incorporation of LWAs has a minor or even negative influence on pore connectivity. In this case, a higher binder porosity with lower aggregate porosity in L-2 results in better water transport properties as compared to L-3 and L-L. On the other hand, the PSD within samples also plays a vital role in determining water vapor transport. Huang et al. [38] concluded that large capillaries and microcracks have a greater impact on moisture transport rates than other pore components. As learned from Fig. 9, L-2 exhibits the highest percentage of pore below 10 μm among LWAGs, which can be another cause for the promoted water transport property. Here, the superior water transport performance observed in LWAGs can offer better thermal stability over sand geopolymer composites by facilitating the thermally induced water vapor, and thus reducing the inner thermal stress, which will be discussed below.

3.1.4. Mechanical strength

The compressive strength of designed samples is determined at the age of 7 and 28 days, and the results are shown in Fig. 11. As expected, the SAG exhibits the highest compressive strength from 7 to 28 days owing to its dense structure. For the LWAG, the optimized mixtures, namely L-2 and L-3, have a higher strength as compared to the unoptimized mixture. This is mainly due to the poor packing in L-L as evidenced by PSD, proving the advantage of packing design for LWAGs considering the mechanical strength. Moreover, L-2 shows a lower early compressive strength at 7 days while a higher compressive strength at a

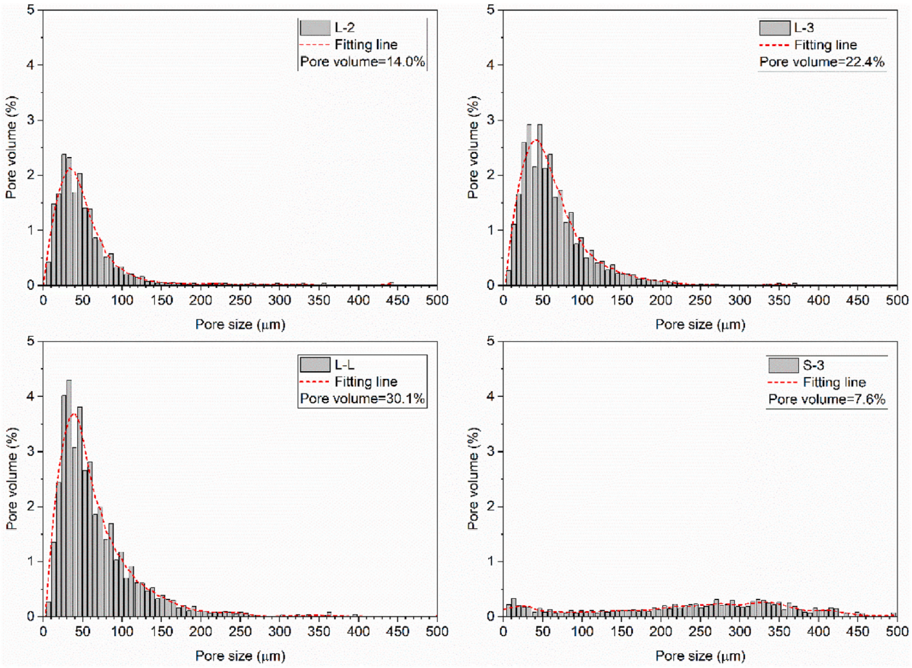

Fig. 9. Pore size distribution of geopolymer composites from Micro-CT scanning.

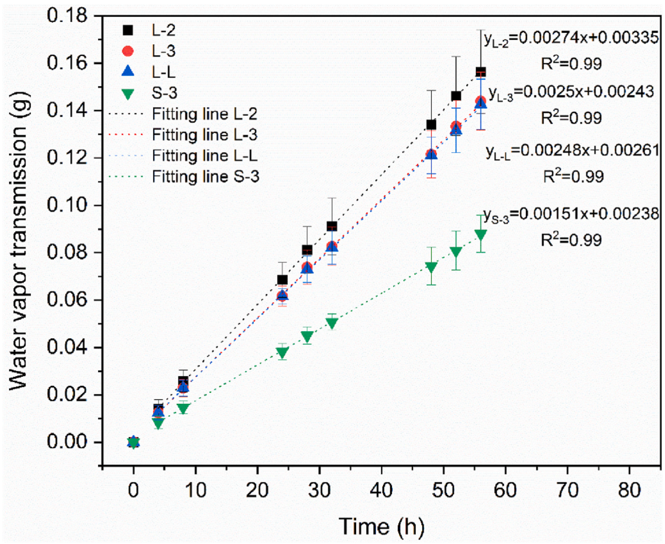

Fig. 10. Water vapor transport in different samples as a function of time duration.

Table 5
Water transport properties, water vapor transmission rate (WVTR), permeability (δ).

Code	Slope (g/h)	WVTR (g/h m^2)	δ (m/s)
L-2	0.00274	1.71	0.0078
L-3	0.0025	1.56	0.0071
L-L	0.00248	1.55	0.0071
S-3	0.00151	0.94	0.0043

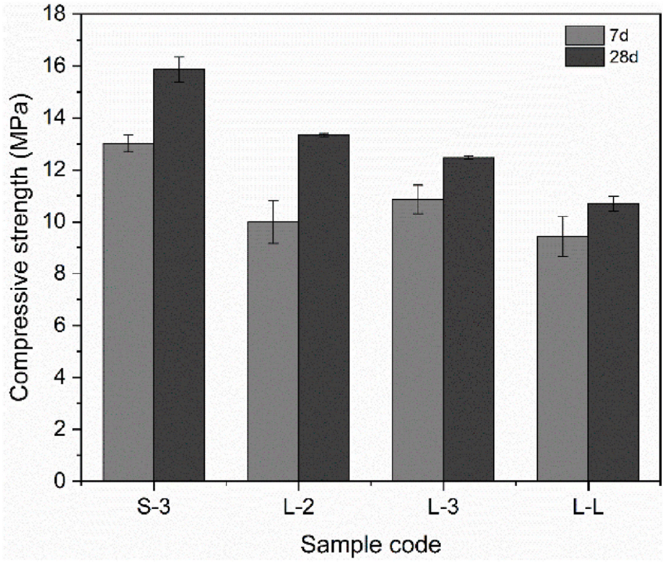

Fig. 11. Compressive strength of sample at 7 and 28 days of curing.

later age when compared to L-3. This should be due to the slow strength development of the geopolymer binder, which is initially weaker than LWA. Therefore, the increasing content of LWAs in L-3 further strengthens the matrix at an early age. While the binder gel takes the dominant role in the compressive behavior at a later age, thus L-2 sample shows the highest strength gain from 7 to 28 days.

3.2. *Heat transfer study*

3.2.1. *Thermo-physical properties*

The thermal-physical properties, including thermal conductivity, thermal diffusion, and volumetric heat capacity are summarized in Table 6. All parameters are measured under constant pressure and volume. The volumetric heat capacity considers the role of bulk density, which is preferable to differentiate the effect of lightweight aggregates and normal sand on the heat gain within the composites. For simplification, the volumetric heat capacity is represented as heat capacity in the following discussion.

The thermal conductivity of prepared geopolymer composites with sand is significantly increased as compared to LWAs. This is primarily due to the high thermal conductivity of regular sand, which largely amplifies the overall thermal conductivity of the geopolymer composite. For LWAG, it is noticed that a higher q value contributes to lower thermal conductivity. In addition, the unoptimized sample L-L exhibits a lower thermal conductivity as compared to L-3. It is because the poor packing in L-L introduces more large pores/voids in the matrix, further reducing the thermal conductivity. In addition to thermal conductivity, SAG also exhibits the highest thermal diffusion and volumetric heat capacity among all the developed composites due to its dense structure. Moreover, among LWAGs, it is noticed that the variation of heat capacity and thermal diffusion is not linearly related to thermal conductivity or bulk density. This discrepancy might be because of the specific pore structure by introducing LWAs. Hence, the obtained thermos-physical properties with specific pore structures are expected to impact the high temperature behavior of geopolymer composites, which will be discussed below.

Lastly, the thermal conductivity versus compressive strength is compared with previous literature in Fig. 12. In accordance with previous studies, the compressive strength of designed LWAGs is found to reduce along with the thermal conductivity. Moreover, it is noted that a higher mechanical strength is obtained in this study as compared to other lightweight geopolymers with similar thermal conductivity. It further proves that the optimized packing model contributes to a compact mixture with homogenously distributed LWAs, enabling a low thermal conductivity with decent compressive strength.

3.2.2. *Temperature contour*

Numerical simulation is employed to study the heat transfer process within different composites as a function of packing design and aggregate type. In the 'CS' model, the binder and aggregates are assigned individual main parameters, including bulk density, thermal conductivity, and heat capacity which are determined as mentioned in the testing method section and summarized in Table 7.

The simulated heat transfer through the L-2 composite as a function of exposure time is extracted and shown as an example in Fig. 13a, and the temperature maps of different composites at 100 min are compared in Fig. 13b. The external heating load is imposed on the perimeters of the simulated models as per experimental setup corresponds to Eq. (14), and a cyclic-shaped temperature distribution can be observed within all composites. In LWAG, the isothermal lines are unevenly distributed, and the isotherms are denser in the area close to the heating source than that in the core area. As compared to L-2, denser isothermal lines are presented in L-3 and L-L, indicating a higher LWA proportion leads to a

Table 6
The thermal conductivity (λ), thermal diffusion (α), and volumetric heat capacity ($C_{p,v}$) of samples.

	λ (W/mK)	St dev	α (mm^2/s)	St dev	$C_{p,v}$ (MJ/m^{3}K)	St dev
L-2	0.2866	0.0036	0.2874	0.0148	0.9986	0.0375
L-3	0.2769	0.0018	0.2443	0.0045	1.1337	0.0133
L-L	0.2498	0.0036	0.2496	0.0072	1.0011	0.0147
S-3	1.4010	0.0151	0.9332	0.0511	1.5043	0.0650

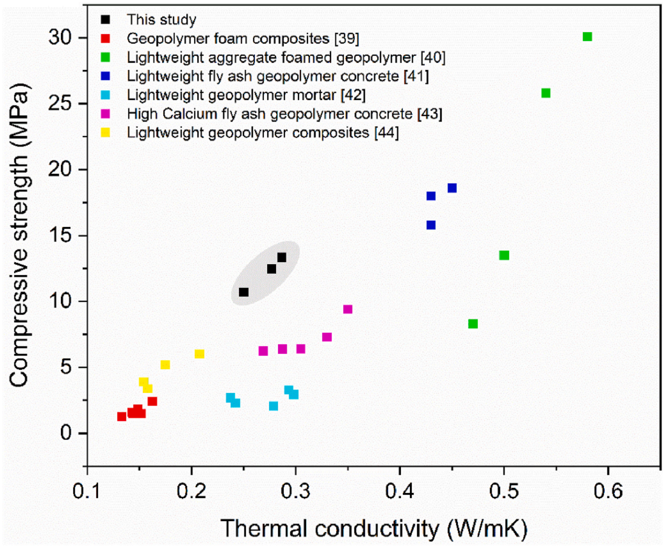

Fig. 12. The relationship between compressive strength and thermal conductivity as compared to other geopolymer based lightweight materials [39–44].

Table 7
Main parameters of the heat transfer simulation.

Sample	Component	ρ_b	λ	$C_{p,v}$
		kg/m^3	W/mK	MJ/m^{3}K
L-2	Composite	1210.0	0.2866	0.9986
	Aggregate	324.2	0.0698	0.2884
	Binder	1961.6	0.4702	1.6011
L-3	Composite	1100.0	0.2769	1.1337
	Aggregate	322.8	0.0698	0.2860
	Binder	2168.9	0.5171	2.2995
L-L	Composite	1090.0	0.2498	1.0011
	Aggregate	318.0	0.0698	0.2735
	Binder	2151.8	0.5133	2.0018
S-3	Composite	1990.0	1.4010	1.5043
	Aggregate	2082.0	0.2024	1.7281
	Binder	1758.0	0.4241	1.1966

larger temperature gradient within the matrix, while a slower temperature gain rate has resulted. Between L-3 and L-L, the isothermal lines in L-L appear relatively more irregular. This is due to the unoptimized packing of L-L, causing a significant difference in thermal conductivity between the binder and aggregates (See Table 7). In comparison, the smaller thermal conductivity difference between sand and geopolymer binder leads to a more evenly distributed isotherm line in S-

3.2.3. *Temperature variation*

The temperature gradients within different composites are compared in Fig. 14, and the simulated temperature change on the surface and at the core of samples is provided in Appendix Fig. A2. For all samples, the temperature gradient increases first and then decreases while the heating temperature is constant. In general, the geopolymers with aggregates diffuse heat slower and show a higher temperature gradient than the standalone binder (Ref) under the same heating conditions. In terms of the packing modulus, L-3 shows the best thermal insulation performance. The dense binder with a relatively low LWA proportion in L-2 leads to a high thermal diffusivity with a small temperature gradient. As for the effect of packing, despite its lower thermal conductivity, L-L exhibits a lower temperature difference as compared to L-3. It is because, the denser matrix obtained in L-3 contributes to a higher heat capacity with a lower thermal diffusivity, meaning a higher thermal inertia to be overcome in L-3 than in L-L. Moreover, it is expected that S-3 shows a smaller temperature gradient than L-3, because of the higher thermal conductivity and faster heat diffusion of sand than that of LWAs.

In summary, the types and packing of aggregates have a combined effect on thermophysical parameters, which have a direct impact on the heat transfer properties of geopolymer composites. The high thermal conductivity and heat capacity of sand result in a more even heat distribution with a small temperature gradient in SAG as compared to LWAGs. In terms of LWAGs, the optimized packing contributes to a high heat capacity and low thermal conductivity, resulting in a low thermal diffusivity with a large temperature gradient. These observed heat transfer properties further influence the high temperature behaviors of geopolymer composites, which is discussed in the next section.

3.3. *High temperature behavior*

It has been well studied that the thermal behavior of geopolymer binder under elevated temperatures is governed by major factors including further geopolymerization, gel dehydration, re-crystallization, and viscous sintering [45–47]. Hence, this section mainly focuses on the interaction between aggregates and geopolymer binder under elevated temperatures, and its further influence on high temperature performance, such as thermal transport properties, microstructural change, volumetric stability, and thermal mechanical evolution.

3.3.1. *Thermal conductivity and microstructural transformation*

The thermal conductivity of the geopolymer composites after high temperature exposure is depicted in Fig. 15. The thermal conductivity of the SAG sample keeps decreasing from 1.401 to 1.005 W/mK. LWAGs show a stable thermal conductivity before 600 °C, following a slightly increase up to 800 °C. The difference in thermal conductivity among LWAGs is insignificant, and the thermal conductivity after 800 °C exposure is proportional to the initial thermal conductivity. Pan et al. [14] reported the thermal conductivity of FA based geopolymer paste during high temperature exposure as summarized in Fig. 15. In comparison, the initial thermal conductivity of LWAGs is lower than FA based geopolymer paste, while that of SAG is much higher, owing to the thermophysical properties of different aggregates as discussed in Section 3.2. Moreover, the thermal conductivity of LWAGs shows a similar but more stable tendency to FA geopolymer paste at high temperatures. Here, the difference between the presented and previous study should mainly result from the aggregate incorporation. The incorporation of LWAs promotes the microstructural stability and subsequently, minimizes the thermal conductivity variation at high temperatures. While the sand incorporation further intensifies the thermally induced microcracking, resulting in a continuous reduction in thermal conductivity. On the other hand, this discrepancy may be raised by the measurement technique. The thermal conductivity at high temperatures might be higher than that of exposed geopolymer due to the presence of thermal radiation upon exposure to heat [48]. In summation, a reasonable variation in thermal conductivity is observed as compared to previously reported results.

The thermally induced microstructure transformation between SAG and LWAG (L-3 and S-3) is compared in Fig. 16. Before being exposed to high temperature, spherical particles can be observed in both L-3 and S-3, representing the unreacted FA. A weak bond between sand and binder gel is noticed in S-3, while it is difficult to identify the ITZ between LWA and gel. At 200 °C, both samples are relatively stable with minor cracks. Noteworthy, owing to the further geopolymerization of the binder, the ITZ in S-3 is refined and becoming insignificant. From 200 to 600 °C, varying degrees of microstructure degradation are detected due to the decomposition of geopolymeric gel as well as the physical interaction between binder gel and aggregates. Two deterioration patterns are differentiated in L-3 and S-3: i) In S-3, drastic structural deterioration is

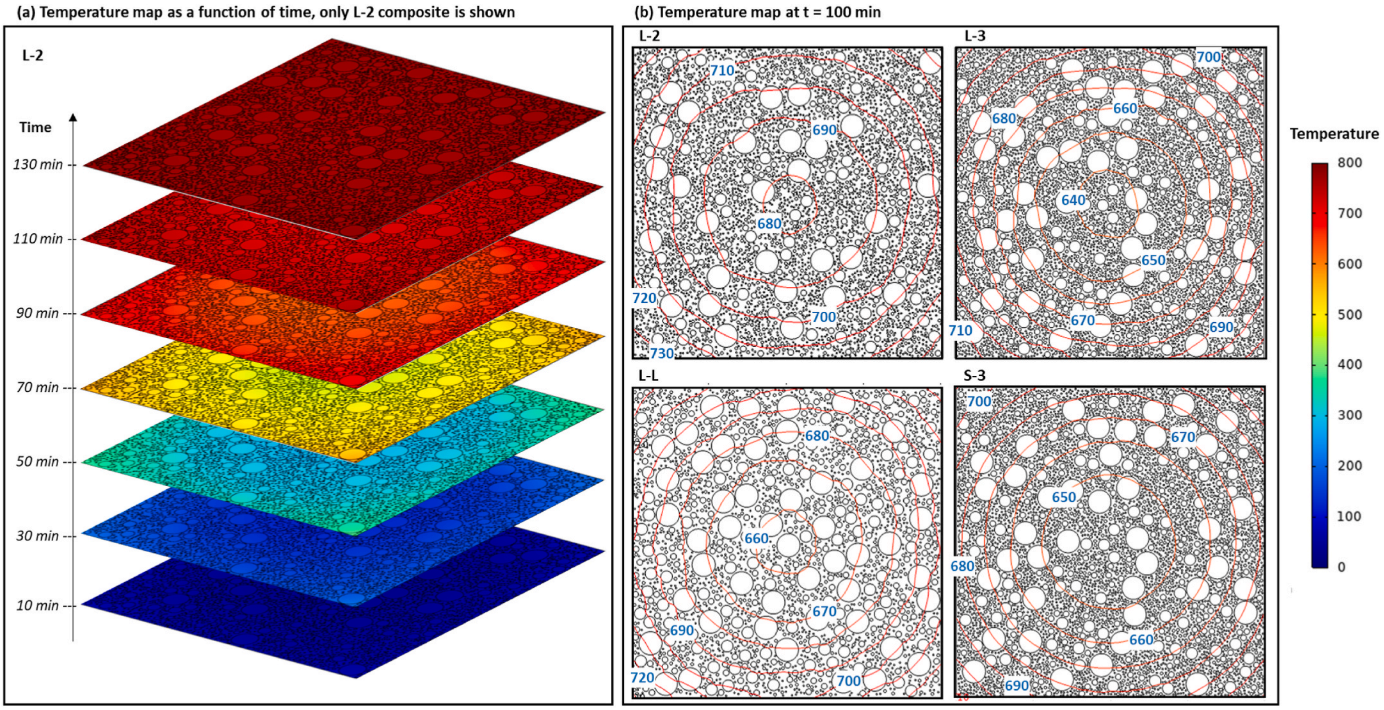

Fig. 13. Heat transfer simulation results (temperature contour) of different samples as a function of time.

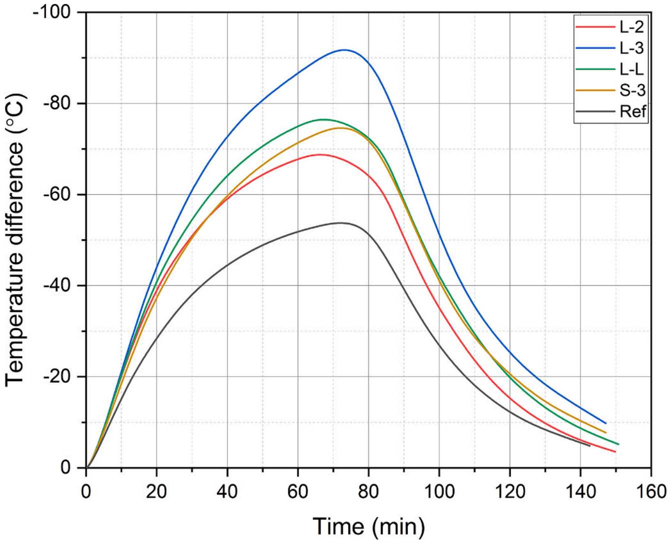

Fig. 14. The temperature gradient within samples between the surface and core.

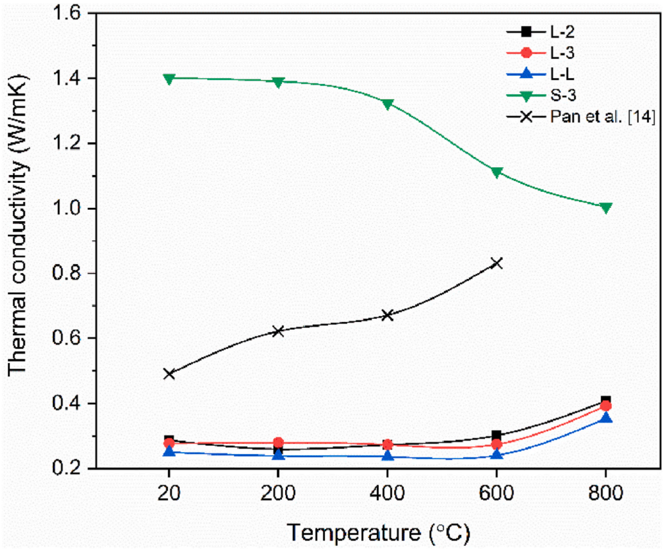

Fig. 15. Thermal conductivity after exposure to elevated temperatures.

noticed in geopolymer binder along sand aggregates, especially at 600 °C. It is known the sand experiences a volumetric expansion owing to β-α quartz transformation at around 573 °C [49]. Simultaneously, the geopolymeric gel is prone to dehydrate and shrink at elevated temperatures [31]. With the significant thermal incompatibility between geopolymer binder and sand, numerous cracks and voids are formed as observed in Fig. 16h. Moreover, sand and unreacted FA particles are increasingly separated from the binder gel, which further weakens the matrix bonding. ii) As for LWAGs, only minor cracks occur to the LWA body along the interface. Interestingly, as compared to S-3, the negative effect of gel shrinkage is mitigated in L-3. This is due to the intrinsic weak mechanical property of LWA. The aggregate body is inevitably damaged during the gel shrinking, while the thermal strain between binder gel and aggregates is reduced, thus largely retaining the binder's structural integrity. At 800 °C, owing to the viscous sintering and re-crystallization of geopolymeric binder [50], the pores of LWAs and cracks in L-3 are partially filled with gel, and the matrix is largely healed and densified. It further explains the rise in thermal conductivity at 800 °C as observed in Fig. 15. While voids between sand and binder gel are still visible in S-3 due to the severe structural deterioration.

3.3.2. Volumetric stability

The linear shrinkage, bulk density, and porosity transformation of samples as a function of temperature are presented in Fig. 17. In general, the thermal evolution of volumetric properties in mixtures with different aggregate type exhibit varied trends. The SAG exhibits a minor linear shrinkage of 0.35% at 800 °C. Kong et al. [11] and Zhang et al. [8] reported that geopolymer mortars with sand or basalt aggregates

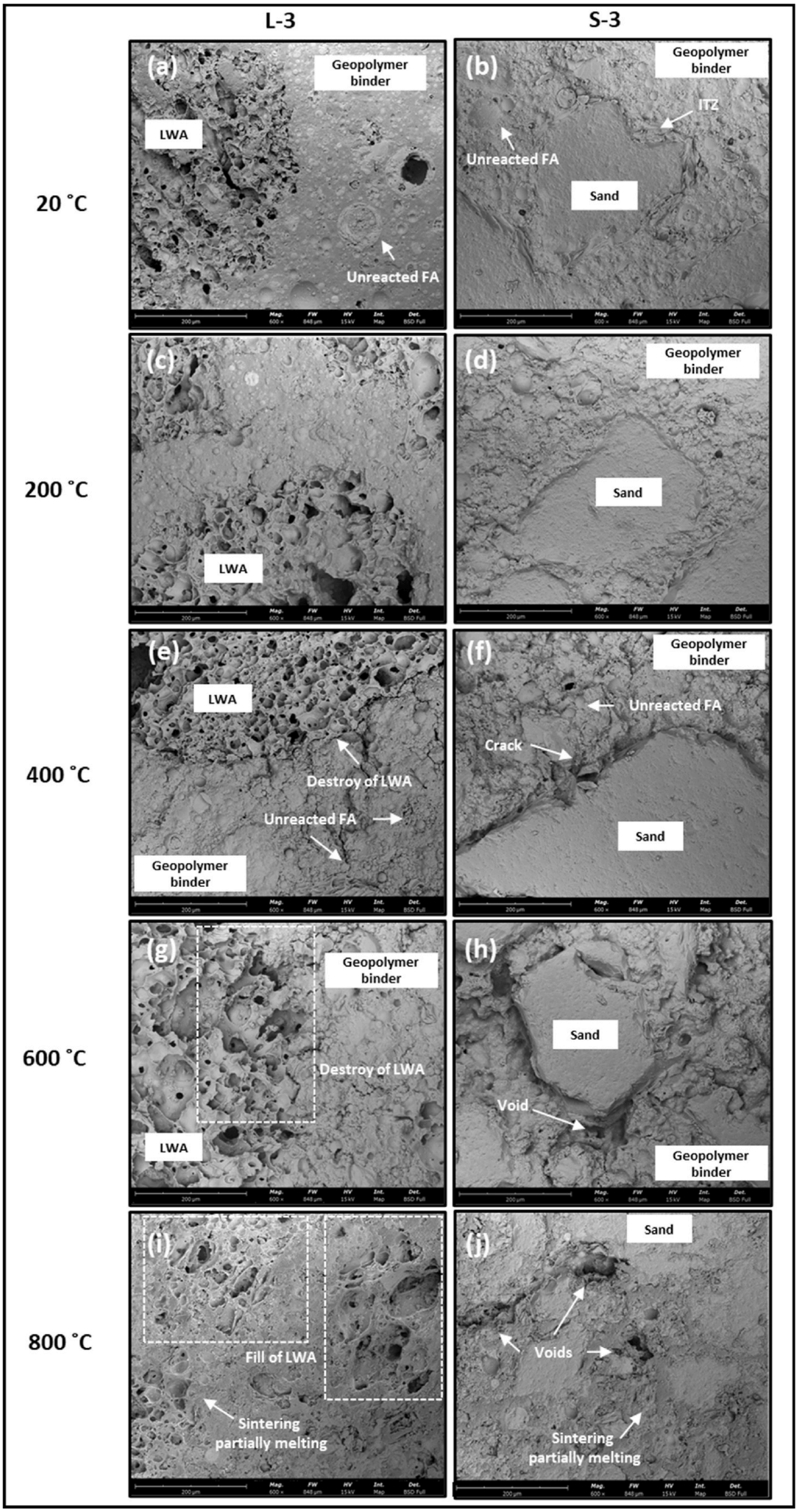

Fig. 16. The microstructure of geopolymer composites exposed to high temperatures.

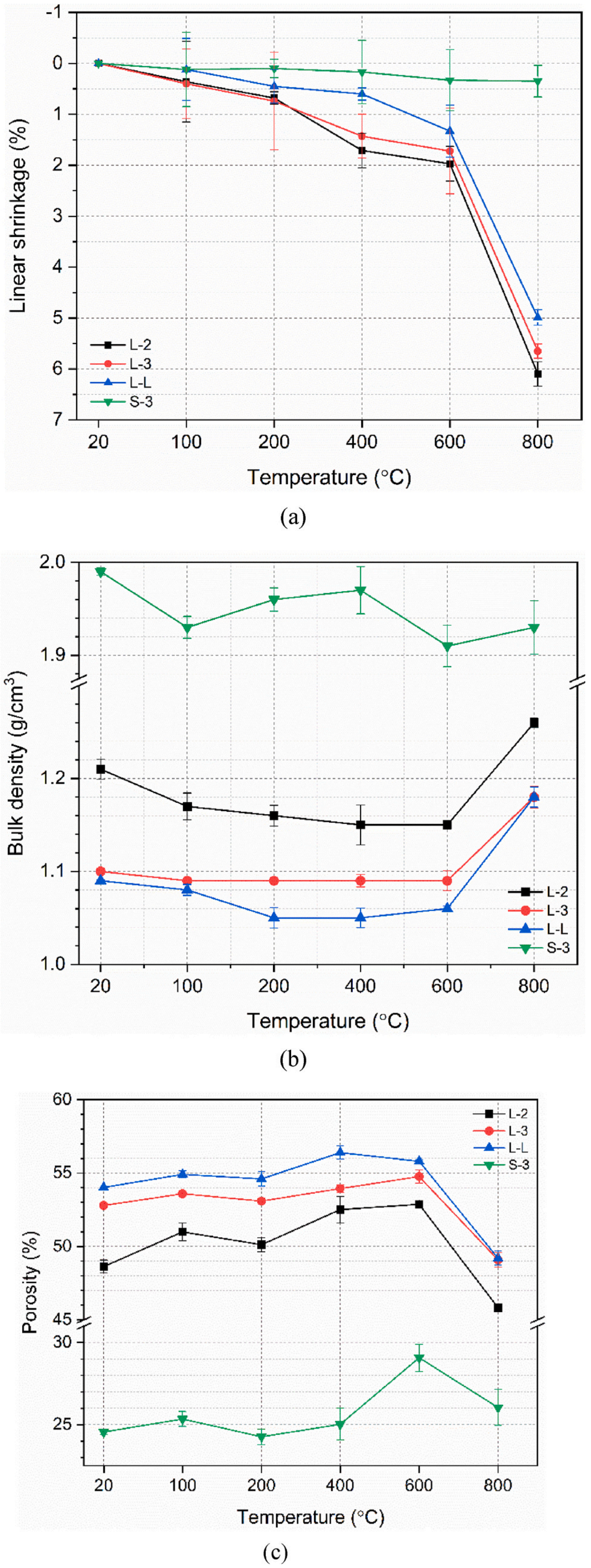

Fig. 17. The variation of (a) linear shrinkage, (b) density, and (c) porosity of geopolymer composites at different temperatures.

experience thermal expansion up to 800 °C, attributed to the thermal incompatibility between geopolymer binder and aggregates. Here, the observed good thermal volumetric stability can be assigned to the optimized sand aggregate packing, which serves as a reinforcing skeleton that can resist thermal deformation. In comparison, LWAGs undergo different degree of thermal shrinkage with the sharpest shrinkage occurs from 600 to 800 °C. This is because, on the one hand, the LWAs are relatively weak, and the thermal shrinkage of binder gel plays a dominate role before 600 °C. On the other hand, as observed in Fig. 16i, the partial melting and viscous sintering of binder at 800 °C fill the pores of LWAs, which is the main cause of the drastic shrinkage. More specifically, it is noticed that unoptimized LWAG as well as LWAG with a higher q value experiences less linear shrinkage. It can be deduced that a coarse pore structure with high porosity or large LWAs fraction is beneficial to alleviate the matrix thermal shrinkage.

As shown in Fig. 17 b and c, the evolution of bulk density and porosity can be an indicator of thermally induced microstructural change, such as crack formation and matrix densification. As compared to LWAGs, despite SAG showing the lowest linear shrinkage up to 800 °C, significant variations in bulk density as well as porosity are observed. The S-3 shows an obvious reduction in bulk density with increased porosity at 100 °C. A similar trend was reported in geopolymer composites with fine pegmatite aggregates [51], indicating the crack formation induced by the drastic water evaporation. From 400 to 600 °C, there is a remarkable drop in bulk density accompanied by increased porosity in S-3. This can be attributed to the sand expansion, which is consistent with SEM results. Then, insignificant matrix densification is noticed at 800 °C, suggesting a diminished healing effect during viscous sintering. The LWAGs exhibit similar trends in bulk density as well as porosity from 20 to 800 °C. Among these, the optimized mixture with a q value of 0.3 shows the best stability before 600 °C. After 600 °C, all the LWAGs undergo significant matrix densification with reduced porosity, further proving the filling effect of viscous gels.

In general, the high stiffness of sand with optimized packing provides decent macro stability at high temperatures. However, at the microstructural level, the conflicting thermal behavior among geopolymer binder and sand aggregates leads to severe microstructural deterioration. On the other hand, the incorporation of LWAs helps to alleviate the thermal mismatch between paste and aggregates thanks to its high permeability and mechanical weakness, resulting in reduced microstructural deterioration.

3.3.3. *Residual compressive strength*

The mechanical strength variation as a function of temperature is depicted in Fig. 18a. A noticeable difference in mechanical strength evolution is observed between SAG and LWAG. All composites show a different degree of strength gain at 100 °C. Then, LWAGs exhibit a strength reduction till 600 °C, following a strength rise at 800 °C. While the compressive strength of S-3 keeps dropping from 100 to 800 °C. Above all, the SAG sample shows the highest mechanical strength before 600 °C, while LWAGs have superior mechanical strength at 800 °C, especially for L-3.

The thermal mechanical strength change ratio in different composites is further compared in Fig. 18b. It is known that the strength gain of geopolymer binder at 100 °C is mainly because of the further geopolymerization [52]. As compared to the remarkable strength gain of 78.4% in SAG, LWAGs only exhibit a slight compressive strength gain. This is because in LWAGs, despite the further geopolymerization that refines the ITZ between binder and aggregates, the poor mechanical property of LWAs largely hinders the strength gain effect. It explains the higher strength gain in L-2 than L-3 due to its higher binder content. Whilst given the high stiffness of sand aggregates, the positive effect of further geopolymerization is more significant in SAG. After 100 °C, the strength evolution in geopolymers is mainly affected by two mechanisms, namely the dehydration/decomposition of binder gel and the

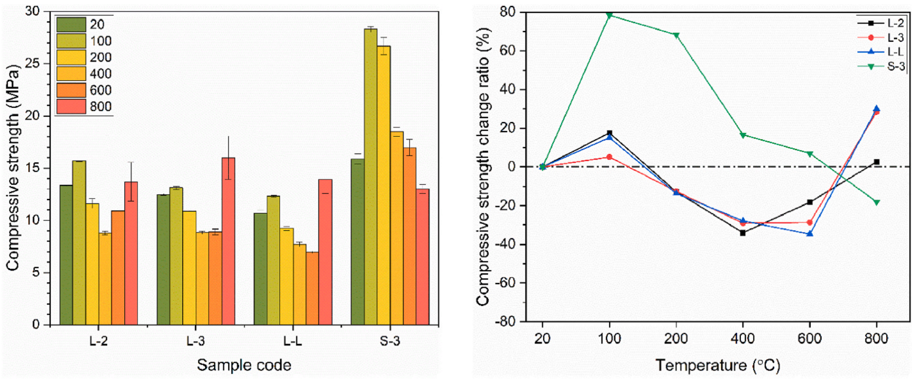

(a) (b)

Fig. 18. (a) The compressive strength and (b) strength change ratio of composites at different temperatures.

thermal interaction between binder gel and aggregates. In general, SAG experiences a more drastic strength deterioration compared to LWAGs from 100 to 800 °C. This is because, on the one hand, the dense matrix with low permeability (see Table 6) gives rise to thermal stress during water evaporation [53]. On the other hand, as detected in SEM, the thermal mismatch among binder shrinkage and sand expansion after 400 °C remarkably damages the matrix with serious cracking and voids formation. In comparison, LWAGs undergo a moderate strength loss till 400 °C, following a strength gain. As discussed above, the decreased strength loss in LWAGs is mainly thanks to the reduced thermal incompatibilities between binder gel and LWAs. In addition, the high permeability in LWAGs contributes to a lower water vapor pressure, hence weakening the matrix damage. Moreover, it is interesting that a higher q value enables a reduced strength loss rate, whilst a prolonged compressive strength loss period till 600 °C is observed in L-3. This likely corresponds to the different heat transfer processes in L-2 and L-3. As discussed in Section 3.2, during the heating process, L-3 exhibits a lower temperature gain rate than L-2, which would certainly alleviate the thermally induced damage. However, the large thermal gradient in L-3 might prolong the effects of thermal deterioration. Beyond 600 °C, strength gains of 2.6%, 28.4%, and 30.0% are noticed in L-2, L-3, and L-L, respectively, attributed to the viscous sintering. The sample with a larger q value exhibits a higher strength gain, which is contributed by the reduced matrix degradation that allows a superior healing effect. The L-3 and L-L show a relatively similar strength gain ratio due to the same gel/aggregate proportion, whilst the optimized matrix exhibits a higher residual strength. In S-3, the strength gain is hindered due to the drastic structural deterioration.

In conclusion, the geopolymer composites with different aggregate types experience a varied strength evolution under elevated temperatures. As compared to SAG, a reduced strength loss from 100 to 400 °C and an obvious strength gain at 800 °C is observed in LWAGs, owing to the higher permeability and lessened thermal incompatibility. In addition, a higher q value not only contributes to lower thermal-induced damage but also slows down the development of strength deterioration. It should be related to its low binder gel/aggregate ratio and specific heat transfer properties during heating.

4. Conclusions and outlook

This study introduces a novel theoretical approach toward the design of high temperature resistant geopolymer composites based on packing optimization. The microstructural formation, as well as thermophysical properties of the designed lightweight aggregate incorporated geopolymer (LWAG), are examined to compare with sand aggregate incorporated geopolymer (SAG). The role of aggregate characteristics in determining the heat transfer process is numerically explored via heat transfer simulation. Ultimately, the interrelationships between the microstructural-thermophysical properties, heat transfer pattern, and high temperature performance are clarified. The following findings can be summarized:

(1) By applying an optimized packing model, the incorporation of lightweight aggregates (LWA) into geopolymer achieves a significantly high porosity ranging from 48.6% to 54.0% as compared to SAG of 24.6%. Among LWAGs, a higher distribution modulus results in a coarser pore structure. Accordingly, a high moisture permeability of around 0.0078 m/s is obtained in LWAG as compared to SAG of 0.0043 m/s. Owing to the rough surface of LWA, the mechanical interlocking effect between LWA and geopolymeric binder contributes to a good binding and compact matrix, resulting in a comparable mechanical strength to that of SAG.

(2) The type and packing design of aggregates significantly affect the thermophysical parameters of geopolymer composites, especially for thermal conductivity and heat capacity. The incorporation of sand into geopolymer composite leads to a high thermal conductivity and heat capacity. In contrast, LWA enables a promising thermal insulation performance. The optimized packing further contributes to a well-packed matrix with high porosity, resulting in a high heat capacity and low thermal diffusivity. When decreasing the distribution modulus from 0.3 to 0.2, higher thermal conductivity and lower heat capacity are resulted due to the reduced aggregate proportion.

(3) The thermal progression development of geopolymer composites is largely influenced by the intrinsic property of aggregates. The optimized packing of sand in geopolymer largely resists the macro-deformation up to 800 °C. But severe microstructural deterioration and strength loss is noticed in SAG due to the drastic matrix incompatibility. In contrast, the incorporation of LWAs results in less thermal destruction with better mechanical stability. However, it ultimately leads to significant shrinkage. Increasing the distribution modulus further alleviates the strength deterioration in LWAGs, attributed to the resulting microstructure and heat transfer pattern.

(4) The distinct thermophysical properties of LWAs and sand significantly vary the heat transfer pattern in geopolymer composites. Sand incorporation results in a fast heat transfer with even temperature distribution in geopolymer composite upon heating. In contrast, the low thermal conductivity of LWAs impedes the inner heat transfer, hence generating a large temperature gradient within the composites. In addition, increasing the distribution modulus reduces the thermal diffusivity and temperature gain rate. It potentially slows down the development of strength

deterioration and eases the mechanical degradation in LWAGs at elevated temperatures.

The presented results build a picture of the progressive evolution of geopolymer composites under elevated temperatures, which offers new insights into the thermal degradation mechanism of geopolymer-based mortar/concrete. The introduced design approach can serve as a framework for advancing high temperature resistant geopolymer composites. It shows potential for using geopolymers in large-scale applications like structural elements and tunnel linings that require heat/fire resistance. Nevertheless, this study primarily focuses on the post-heating behavior of geopolymer composites. Future research concerning the in-situ thermal behavior characterization is imperative to achieve a more comprehensive grasp of the thermal performance of geopolymer composites.

Declaration of competing interest

The authors declare that they have no known competing financial interests or personal relationships that could have appeared to influence the work reported in this paper.

Data availability

Data will be made available on request.

Appendix

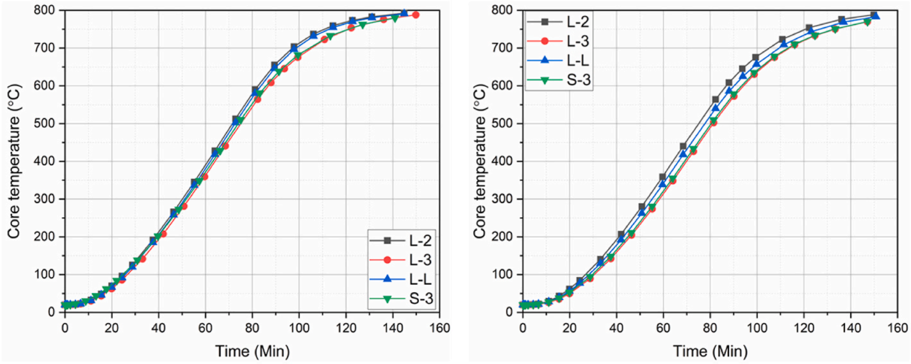

(a)

(b)

Fig. A1. Validation of heat transfer simulation (a: BS model, b: CS model)

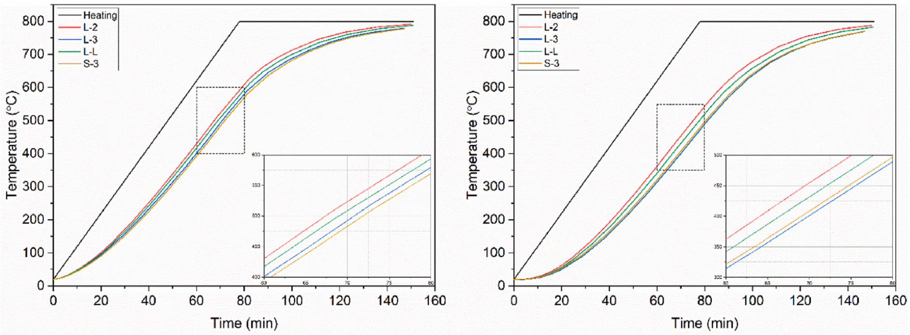

(a)

(b)

Fig. A2. The temperature change of (a) the surface (0 mm) and (b) the core (20 mm) for different samples

References

[1] P. Duxson, A. Fernández-Jiménez, J.L. Provis, G.C. Lukey, A. Palomo, J.S.J. van Deventer, Geopolymer technology: the current state of the art, J. Mater. Sci. 42 (2007) 2917–2933, https://doi.org/10.1007/s10853-006-0637-z.

[2] J.L. Provis, S.A. Bernal, Geopolymers and related alkali-activated materials, Annu. Rev. Mater. Res. 44 (2014) 299–327, https://doi.org/10.1146/annurev-matsci-070813-113515.

[3] J.L. Provis, A. Palomo, C. Shi, Advances in understanding alkali-activated materials, Cement Concr. Res. 78 (2015) 110–125, https://doi.org/10.1016/j.cemconres.2015.04.013.

[4] C.R. Kaze, G.L. Lecomte-Nana, E. Kamseu, P.S. Camacho, A.S. Yorkshire, J. L. Provis, M. Duttine, A. Wattiaux, U.C. Melo, Mechanical and physical properties of inorganic polymer cement made of iron-rich laterite and lateritic clay: a comparative study, Cement Concr. Res. 140 (2021), 106320, https://doi.org/10.1016/j.cemconres.2020.106320.

[5] H. Lin, H. Liu, Y. Li, X. Kong, Properties and reaction mechanism of phosphoric acid activated metakaolin geopolymer at varied curing temperatures, Cement Concr. Res. 144 (2021), 106425, https://doi.org/10.1016/j.cemconres.2021.106425.

[6] D.L.Y. Kong, J.G. Sanjayan, K. Sagoe-Crentsil, Comparative performance of geopolymers made with metakaolin and fly ash after exposure to elevated temperatures, Cement Concr. Res. 37 (2007) 1583–1589, https://doi.org/10.1016/j.cemconres.2007.08.021.

[7] A. Fernández-Jiménez, A. Palomo, J.Y. Pastor, A. Martín, New cementitious materials based on alkali-activated fly ash: performance at high temperatures, J. Am. Ceram. Soc. 91 (2008) 3308–3314, https://doi.org/10.1111/j.1551-2916.2008.02625.x.

[8] H.Y. Zhang, V. Kodur, B. Wu, L. Cao, F. Wang, Thermal behavior and mechanical properties of geopolymer mortar after exposure to elevated temperatures, Construct. Build. Mater. 109 (2016) 17–24, https://doi.org/10.1016/j.conbuildmat.2016.01.043.

[9] A. Nazari, A. Bagheri, J.G. Sanjayan, M. Dao, C. Mallawa, P. Zannis, S. Zumbo, Thermal shock reactions of Ordinary Portland cement and geopolymer concrete: microstructural and mechanical investigation, Construct. Build. Mater. 196 (2019) 492–498, https://doi.org/10.1016/j.conbuildmat.2018.11.098.

[10] S. Çelikten, M. Sarıdemir, İ. Özgür Deneme, Mechanical and microstructural properties of alkali-activated slag and slag + fly ash mortars exposed to high temperature, Construct. Build. Mater. 217 (2019) 50–61, https://doi.org/10.1016/j.conbuildmat.2019.05.055.

[11] D.L.Y. Kong, J.G. Sanjayan, Effect of elevated temperatures on geopolymer paste, mortar and concrete, Cement Concr. Res. 40 (2010) 334–339, https://doi.org/10.1016/j.cemconres.2009.10.017.

[12] D.L.Y. Kong, J.G. Sanjayan, Damage behavior of geopolymer composites exposed to elevated temperatures, Cement Concr. Compos. 30 (2008) 986–991, https://doi.org/10.1016/j.cemconcomp.2008.08.001.

[13] W.D.A. Rickard, G.J.G. Gluth, K. Pistol, In-situ thermo-mechanical testing of fly ash geopolymer concretes made with quartz and expanded clay aggregates, Cement Concr. Res. 80 (2016) 33–43, https://doi.org/10.1016/j.cemconres.2015.11.006.

[14] Z. Pan, Z. Tao, Y.-F. Cao, R. Wuhrer, Measurement and prediction of thermal properties of alkali-activated fly ash/slag binders at elevated temperatures, Mater. Struct. 51 (2018) 108, https://doi.org/10.1617/s11527-018-1233-9.

[15] N.A. Jaya, Correlation between pore structure, compressive strength and thermal conductivity of porous metakaolin geopolymer, Construct. Build. Mater. (2020) 12.

[16] J.G. Deutou Nemaleu, C.R. Kaze, E.A. Belela, G.L. Lecomte-Nana, E. Kamseu, V. M. Sglavo, C. Leonelli, Refractory ceramics bonds from potassium-based inorganic polymer for advanced applications: crystalline phase changes and descriptive microstructure, Ceram. Int. 48 (2022) 21579–21588, https://doi.org/10.1016/j.ceramint.2022.04.130.

[17] H.J.H. Brouwers, H.J. Radix, Self-compacting concrete: theoretical and experimental study, Cement Concr. Res. 35 (2005) 2116–2136, https://doi.org/10.1016/j.cemconres.2005.06.002.

[18] M. Hunger, An Integral Design Concept for Ecological Self-Compacting Concrete, University of Technology, Eindhoven, 2010.

[19] R. Yu, P. Spiesz, H.J.H. Brouwers, Development of an eco-friendly Ultra-High Performance Concrete (UHPC) with efficient cement and mineral admixtures uses, Cement Concr. Compos. 55 (2015) 383–394, https://doi.org/10.1016/j.cemconcomp.2014.09.024.

[20] R. Yu, P. Spiesz, H.J.H. Brouwers, Mix design and properties assessment of ultra-high performance fibre reinforced concrete (UHPFRC), Cement Concr. Res. 56 (2014) 29–39, https://doi.org/10.1016/j.cemconres.2013.11.002.

[21] G. Hüsken, H.J.H. Brouwers, A new mix design concept for earth-moist concrete: a theoretical and experimental study, Cement Concr. Res. 38 (2008) 1246–1259, https://doi.org/10.1016/j.cemconres.2008.04.002.

[22] G. (Götz) Hüsken, A Multifunctional Design Approach for Sustainable Concrete: with Application to Concrete Mass Products, 2010, https://doi.org/10.6100/IR693348.

[23] Q.L. Yu, P. Spiesz, H.J.H. Brouwers, Ultra-lightweight concrete: conceptual design and performance evaluation, Cement Concr. Compos. 61 (2015) 18–28, https://doi.org/10.1016/j.cemconcomp.2015.04.012.

[24] Q.L. Yu, P. Spiesz, H.J.H. Brouwers, Development of cement-based lightweight composites – Part 1: mix design methodology and hardened properties, Cement Concr. Compos. 44 (2013) 17–29, https://doi.org/10.1016/j.cemconcomp.2013.03.030.

[25] P. Spiesz, Q.L. Yu, H.J.H. Brouwers, Development of cement-based lightweight composites – Part 2: durability-related properties, Cement Concr. Compos. 44 (2013) 30–40, https://doi.org/10.1016/j.cemconcomp.2013.03.029.

[26] Q.L. Yu, H.J.H. Brouwers, Development of a self-compacting gypsum-based lightweight composite, Cement Concr. Compos. 34 (2012) 1033–1043, https://doi.org/10.1016/j.cemconcomp.2012.05.004.

[27] Y. Luo, S.H. Li, K.M. Klima, H.J.H. Brouwers, Q. Yu, Degradation mechanism of hybrid fly ash/slag based geopolymers exposed to elevated temperatures, Cement Concr. Res. 151 (2022), 106649, https://doi.org/10.1016/j.cemconres.2021.106649.

[28] J.E. Funk, D.R. Dinger, Predictive Process Control of Crowded Particulate Suspensions: Applied to Ceramic Manufacturing, Kluwer Academic Publishers, Boston, the United States, 1994.

[29] P.H.R. Borges, L.F. Fonseca, V.A. Nunes, T.H. Panzera, C.C. Martuscelli, Andreasen particle packing method on the development of geopolymer concrete for civil engineering, J. Mater. Civ. Eng. 26 (2014) 692–697, https://doi.org/10.1061/(ASCE)MT.1943-5533.0000838.

[30] X. Gao, Q.L. Yu, H.J.H. Brouwers, Assessing the porosity and shrinkage of alkali activated slag-fly ash composites designed applying a packing model, Construct. Build. Mater. 119 (2016) 175–184, https://doi.org/10.1016/j.conbuildmat.2016.05.026.

[31] Y. Luo, K.M. Klima, H.J.H. Brouwers, Q. Yu, Effects of ladle slag on Class F fly ash geopolymer: reaction mechanism and high temperature behavior, Cement Concr. Compos. 129 (2022), 104468, https://doi.org/10.1016/j.cemconcomp.2022.104468.

[32] ISO/DIS22007-2, Determination of Thermal Conductivity and Thermal Diffusivity, Part 2: Transient Plane Heat Source (Hot Disc) Method, International Organization for Standardization, 2008.

[33] ASTM E96/E96M-21, Standard Test Methods for Water Vapor Transmission of Materials Standard Test Methods for Gravimetric Determination of Water Vapor Transmission Rate of Materials, ASTM International, 2021, https://doi.org/10.1520/E0096_E0096M-21.

[34] British Standards Institution: London, Methods of Testing Cement, 2016. Part 1, Part 1.

[35] COMSOL 5.6, COMSOL Multiphysics Reference Manual, 2020.

[36] D.S. Smith, A. Alzina, J. Bourret, B. Nait-Ali, F. Pennec, N. Tessier-Doyen, K. Otsu, H. Matsubara, P. Elser, U.T. Gonzenbach, Thermal conductivity of porous materials, J. Mater. Res. 28 (2013) 2260–2272, https://doi.org/10.1557/jmr.2013.179.

[37] B. Budiansky, Thermal and thermoelastic properties of isotropic composites, J. Compos. Mater. 4 (1970) 286–295, https://doi.org/10.1177/002199837000400301.

[38] Q. Huang, Z. Jiang, X. Gu, W. Zhang, B. Guo, Numerical simulation of moisture transport in concrete based on a pore size distribution model, Cement Concr. Res. 67 (2015) 31–43, https://doi.org/10.1016/j.cemconres.2014.08.003.

[39] Y.X. Chen, K.M. Klima, H.J.H. Brouwers, Q. Yu, Effect of silica aerogel on thermal insulation and acoustic absorption of geopolymer foam composites: the role of aerogel particle size, Compos. B Eng. 242 (2022), 110048, https://doi.org/10.1016/j.compositesb.2022.110048.

[40] M.Y.J. Liu, U.J. Alengaram, M.Z. Jumaat, K.H. Mo, Evaluation of thermal conductivity, mechanical and transport properties of lightweight aggregate foamed geopolymer concrete, Energy Build. 72 (2014) 238–245, https://doi.org/10.1016/j.enbuild.2013.12.029.

[41] A. Wongsa, Y. Zaetang, V. Sata, P. Chindaprasirt, Properties of lightweight fly ash geopolymer concrete containing bottom ash as aggregates, Construct. Build. Mater. 111 (2016) 637–643, https://doi.org/10.1016/j.conbuildmat.2016.02.135.

[42] A. Wongsa, V. Sata, B. Nematollahi, J. Sanjayan, P. Chindaprasirt, Mechanical and thermal properties of lightweight geopolymer mortar incorporating crumb rubber, J. Clean. Prod. 195 (2018) 1069–1080, https://doi.org/10.1016/j.jclepro.2018.06.003.

[43] P. Posi, C. Ridtirud, C. Ekvong, D. Chammanee, K. Janthowong, P. Chindaprasirt, Properties of lightweight high calcium fly ash geopolymer concretes containing recycled packaging foam, Construct. Build. Mater. 94 (2015) 408–413, https://doi.org/10.1016/j.conbuildmat.2015.07.080.

[44] F. Colangelo, G. Roviello, L. Ricciotti, V. Ferrándiz-Mas, F. Messina, C. Ferone, O. Tarallo, R. Cioffi, C.R. Cheeseman, Mechanical and thermal properties of lightweight geopolymer composites, Cement Concr. Compos. 86 (2018) 266–272, https://doi.org/10.1016/j.cemconcomp.2017.11.016.

[45] W. Tu, M. Zhang, Behaviour of alkali-activated concrete at elevated temperatures: a critical review, Cement Concr. Compos. 138 (2023), 104961, https://doi.org/10.1016/j.cemconcomp.2023.104961.

[46] M. Lahoti, K.H. Tan, E.-H. Yang, A critical review of geopolymer properties for structural fire-resistance applications, Construct. Build. Mater. 221 (2019) 514–526, https://doi.org/10.1016/j.conbuildmat.2019.06.076.

[47] I. Hager, M. Sitarz, K. Mróz, Fly-ash based geopolymer mortar for high-temperature application – effect of slag addition, J. Clean. Prod. 316 (2021), 128168, https://doi.org/10.1016/j.jclepro.2021.128168.

[48] D.S. Smith, A. Alzina, J. Bourret, B. Nait-Ali, F. Pennec, N. Tessier-Doyen, K. Otsu, H. Matsubara, P. Elser, U.T. Gonzenbach, Thermal conductivity of porous materials, J. Mater. Res. 28 (2013) 2260–2272, https://doi.org/10.1557/jmr.2013.179.

[49] J.D. Axe, G. Shirane, Study of the $\alpha - \beta$ quartz phase transformation by inelastic neutron scattering, Phys. Rev. B 1 (1970) 342–348, https://doi.org/10.1103/PhysRevB.1.342.

[50] Y. Luo, H.J.H. Brouwers, Q. Yu, Understanding the gel compatibility and thermal behavior of alkali activated Class F fly ash/ladle slag: the underlying role of Ca availability, Cement Concr. Res. 170 (2023), 107198, https://doi.org/10.1016/j.cemconres.2023.107198.

[51] A. Nana, R. Cyriaque Kaze, T. Salman Alomayri, H. Suliman Assaedi, J.G. Nemaleu Deutou, J. Ngouné, H. Kouamo Tchakouté, E. Kamseu, C. Leonelli, Innovative porous ceramic matrices from inorganic polymer composites (IPCs): microstructure and mechanical properties, Construct. Build. Mater. 273 (2021), 122032, https://doi.org/10.1016/j.conbuildmat.2020.122032.

[52] Z. Pan, J.G. Sanjayan, B.V. Rangan, An investigation of the mechanisms for strength gain or loss of geopolymer mortar after exposure to elevated temperature, J. Mater. Sci. 44 (2009) 1873–1880, https://doi.org/10.1007/s10853-009-3243-z.

[53] M. Guerrieri, J.G. Sanjayan, Behavior of combined fly ash/slag-based geopolymers when exposed to high temperatures, Fire Mater. 34 (2010) 163–175, https://doi.org/10.1002/fam.1014.

List of symbols

φ: Porosity, %
ρ: Density, g/cm^3
λ: Thermal conductivity, W/mK
α: Thermal diffusion, mm^2/s
$C_{p,v}$: Volumetric heat capacity, MJ/m^{3}K
WVTR: Water vapor transmission rate, g/h m^2
δ: Permeability, m/s
V: Volume, cm^3
m: Mass, g
A: Area, mm^2
d: Diameter, mm